

Research Article

Influence of Deviatoric Stress on the Deformation and Damage Evolution of Surrounding Rock under Unloading Conditions

Gongyu Hou,^{1,2} Jinping Liang ,¹ Haoyong Jing,¹ Jinxin Tan,¹ Yongkang Zhang,¹ Xi Yang,¹ and Xin Xie¹

¹School of Mechanics and Civil Engineering, China University of Mining and Technology, Beijing 100083, China

²School of Mining Engineering and Geology, Xinjiang Institute of Engineering, Urumqi 830091, China

Correspondence should be addressed to Jinping Liang; bqt1800605051@student.cumtb.edu.cn

Received 7 January 2020; Revised 24 June 2020; Accepted 17 August 2020; Published 4 September 2020

Academic Editor: Yuri S. Karinski

Copyright © 2020 Gongyu Hou et al. This is an open access article distributed under the Creative Commons Attribution License, which permits unrestricted use, distribution, and reproduction in any medium, provided the original work is properly cited.

The study of the deformation and damage evolution behaviour of surrounding rock under excavation unloading conditions is of vital importance for a deep understanding of the mechanism of roadway failure. In this study, unloading testing using a partially hollow thick-walled cylinder cement mortar specimen with dimensions of 280 mm (height) × 200 mm (outer diameter) × 60 mm (inner diameter) and a solid height of 60 mm at the bottom was performed to investigate the deformation response and damage failure evolution characteristics of the surrounding rock. The experimental results showed that the higher deviatoric stress level accelerated the damage development caused by the unloading effect and improved the expansion rate of the internal cracks, which led to a higher radial strain rate, total strain, and acoustic emission hits. When deviatoric stress increased to a relatively higher level, the radial strain rates were highly unstable, and the surrounding rock near or at the opening free surface was damaged locally and regionally. During the failure process of the specimen, the generation of the deformation and damage in the unloading stage was more alive (as indicated by the growth rate). Nevertheless, the main deformation and damage to the surrounding rock were generated and accumulated in the maintaining stage after unloading.

1. Introduction

Tunnel/roadway engineering construction is an unloading process in a three-dimensional state. With the removal of radial stress and the increase of tangential stress, this process will cause varying degrees of disturbance to an in situ stress field. The disturbed rock masses near or at an opening cave surface often suffer from unloading and creep that can result in rock spalling [1], large squeezing deformation [2], and rock bursting [3–5] during or after an excavation, which could cause serious injuries for underground engineering facilities and workers [6]. A large number of studies have shown that evaluation of the performance of rock damage thresholds, that is, crack closure, crack initiation, and crack damage stresses, is significantly affected by different loading conditions and rock internal structure [7–9]. Clearly, it is vital to study the deformation, failure, and damage evolution of roadway surrounding rocks under unloading conditions.

Owing to the particularity and complexity of underground engineering, the in situ measurement of the rock mass is difficult and the test conditions are not generally available, especially in a deep-buried area. Therefore, in the past few decades, researchers have carried out a large number of theoretical studies [10], numerical simulations [11, 12], and laboratory scale experiments [13–15] to study the rock mechanics and damage failure evolution. Using grain-based distinct element model, Mahdi et al. [11] studied microcracking behaviour of precracked Barre granite. Weng et al. [13] investigated the stability of underground excavations under high in situ stress conditions, and several rock samples with a minitunnel were prepared and subjected to monotonic axial and coupled static–dynamic loading until failure. Munoz et al. [14] investigated the effects of cyclic loading on the deformational characteristics of both the nonlocalized damage zone (NLDZ) and the localized damage zone (LDZ) of rock in the postpeak regime. At

present, much attention has been paid to the study of damage and failure mechanism by AE techniques.

After acoustic emission (AE) techniques were first introduced into rock mechanics studies [16] and the Kaiser effect was discovered [17], the AE techniques began to be applied to investigate earthquake [18], in situ stress measurement [19], determination of fracture initiation stress [20], and rock burst prediction [21]. Focusing on the damage evaluation, Kim et al. [20] compared two damage evaluation methods (stress-strain and AE) and suggested that AE methods were the best choice for damage estimation. Yang et al. [22] obtained the damage and failure evolution characteristics of limestone under triaxial confining pressure. Based on AE parameters and their determination methods, Zhang et al. [23] established damage variables and compared the AE characteristics of rock salt, granite, and marble during damage process. These studies play an important role in understanding the mechanical behaviour of surrounding rock and maintaining the stability of surrounding rock.

To simulate the stress state of rock mass in roadway excavation more effectively, researchers proposed a method to evaluate the stability of circular roadway by using thick-walled cylindrical (TWC) structure model specimens [24, 25]. This was a simple and reliable test method to investigate the effect of roadway excavation, which can simulate the hoop effect and stress gradient of roadway. It has been widely used in laboratory tests to study the mechanical response and supporting characteristics of rock mass [26–31], which greatly promoted the understanding of roadway/tunnel failure mechanism. Due to the difficulty of system development, most previous studies used this structural model to study damage of roadway under loading conditions, and few researchers carried out damage and strength studies under unloading conditions. Nevertheless, few experimental studies focused on the deformation, damage failure mechanism, and AE characteristics of the surrounding rock during or after an excavation unloading. Therefore, a series of unloading tests for partially hollow thick-walled cylinder (PHTWC) cement mortar specimens were carried out using the roadway/tunnel excavation unloading model testing system, which combined with the strain test system and acoustic emission monitoring system. The deformations at different space-time positions of the surrounding rock and the time-frequency-domain characteristics of the AE signals, for example, the AE hits, amplitude, and frequency, were monitored during the entire test process. The effects of different in situ stress levels on the deformation response and the damage failure evolution characteristics of the surrounding rock after excavation were analyzed according to the experimental results.

2. Materials and Methods

2.1. Testing Method. In the laboratory, the emphasis was on studying the degree of influence of the secondary stress field on the surrounding rock deformation and the damage after being removed by an excavated body. The process of roadway excavation unloading was simulated “actually.” The

“actually” term meant that the mechanical process and the principle of this modeling testing were in accordance with the simplification of the mechanical model of the elastic-plastic solution of the circular roadway at the time of testing. The roadway excavation was the process of the “excavated body” being taken out. After excavation, the original stress value dropped to zero and the surrounding rock shrank and deformed.

2.2. Testing System. A roadway/tunnel excavation unloading model testing system that was equipped with a strain measurement system and an AE measurement system was used to achieve the simulation of the in situ stress environment and the roadway excavation. The testing system was also used to investigate the deformation and AE response of the surrounding rock during excavation [29, 31], as shown in Figure 1. It should be noted that the testing system used in this research could achieve independent loading and unloading for the axial, external, and internal stresses. During the test, the inner and outer cavities of the specimen were isolated with rubber sleeve and filled with silicone oil. Through the independent control of the servo valve in the inner and outer cavities, the pipe connecting the inner and outer cavities was pressurized to achieve the independent control of the internal and external pressure. The internal pressure relief process was completed by sending a negative opening command to the corresponding servo valve through the controller.

The static strain gauge (model DH3818Y) used in this study (see Figure 1(b)), equipped with a 24-bit $\Sigma - \Delta$ (A/D) analog-to-digital converter, could achieve continuous and accurate dynamic and static sampling. The storage battery continuously supplied power to the strain gauge, avoiding the noise caused by the AC power supply during the test. Eight strain gauges (numbered #1 to #8) were distributed in different positions inside the specimen to obtain radial strain of the corresponding locations, as shown in Figure 2(a).

Acoustic emission acquisition equipment (model DS5-8B) was used to collect waveform and state information of 8 channels synchronously in real time (Figure 1(c)). Four cylindrical high oil pressure resistant AE broadband ceramic sensors (model RS-5A) with operating frequency range from 50 kHz to 100 kHz were mounted on the outer wall of the specimen, as shown in Figure 2. As a coupling agent, silicone grease reduced the signal attenuation and enhanced the signal transmission between the specimen and sensor by coating on the contact between them. The trigger threshold and the sampling rate were set to 30 dB and 3 MHz/s, respectively. Therefore, the AE response could be obtained effectively during the process of roadway excavation.

2.3. Specimen Preparation. The PHTWC specimens had a height of 280 mm, an outer diameter of 200 mm, and an inner diameter of 60 mm, and the specimens were made of cement mortar material. To create an unexcavated rock mass ahead of the excavation face, a solid with a height of 60 mm was left at the bottom of the specimens. That is, the hollow height was 220 mm (Figure 3). Core specimens

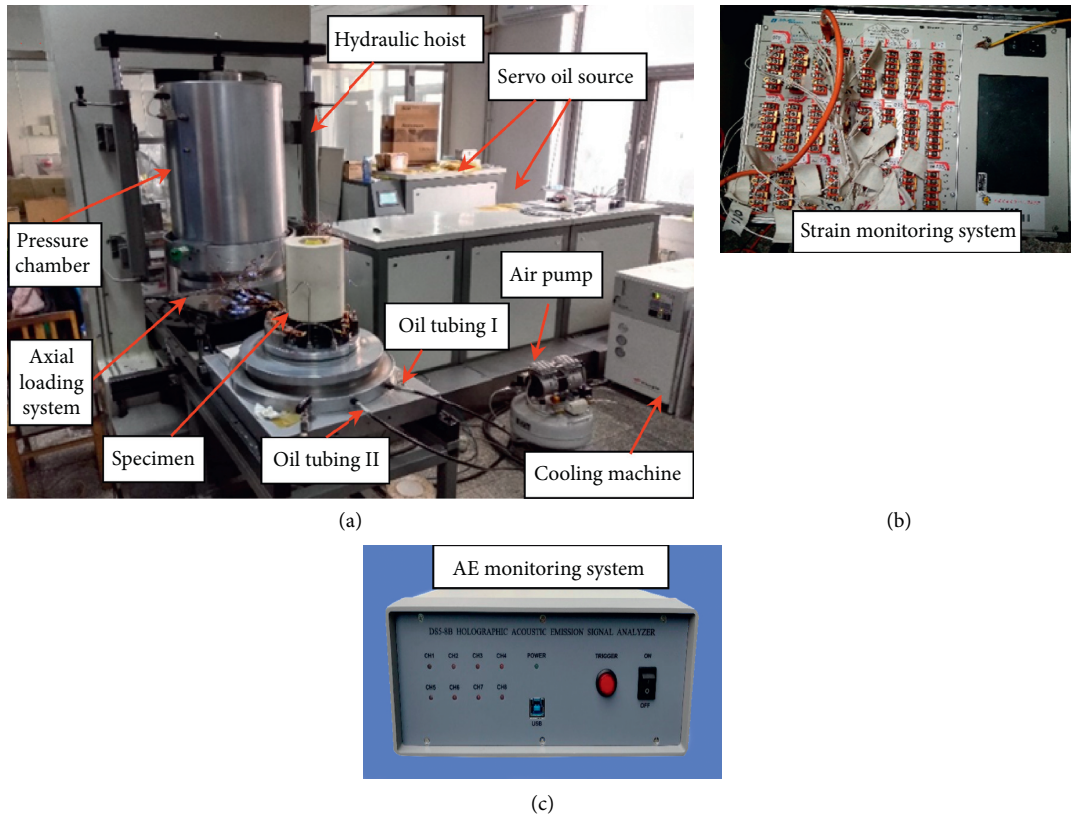


FIGURE 1: Illustration of the tunnel excavation unloading test system: (a) the unloading test machine; (b) the strain monitoring system; (c) the AE monitoring system.

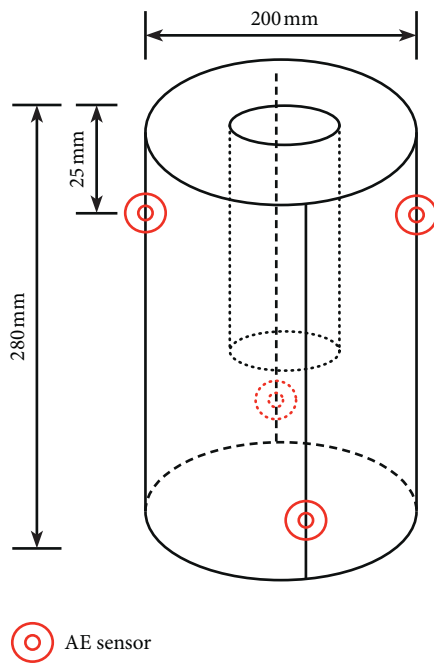


FIGURE 2: Sketch of the AE sensors arrangement.

($\varnothing 50 \times 100$ mm) that were made of cement mortar with the same mix ratio as the PHTWC samples were tested. It was found that the mechanical properties of the core specimens

were similar to those of the sandstone. The physical and mechanical parameters of cement mortar and sandstone are shown in Table 1.

2.4. Testing Program. The axial stress and internal and external confining stresses were increased to the designed levels (10, 20, and 30 MPa) with a constant loading rate of 0.1 MPa/s, following the experimental paths plotted in Figure 4, held on 10 min to allow for stress field homogenisation, then, released internal pressure to produce the difference of external stress and internal stress (hereafter called deviatoric stress), created free surface around the cave, and, finally, held on 8 min to investigate the deformation and AE response after unloading.

3. Experiment Results

3.1. Characteristics Analysis of Fracture. In Figure 5, photographs of three typical representative specimens corresponding to the initial confining stress level can be observed. The figure illustrates the fact that a relatively high stress level triggered the failure. When the stresses were 10 MPa and 20 MPa, the coalescence of fractures and faults on the macroscopic scale occurred. In contrast, no large dilation and volume changes of the surrounding rock appeared toward the direction of the opening free surface induced by stress. When the stress increased to 30 MPa, this resulted in a

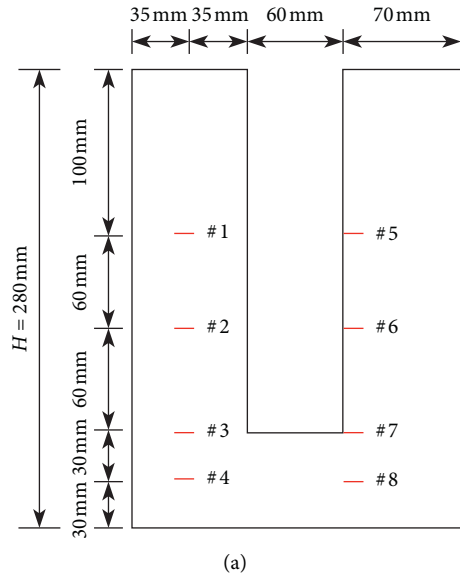


FIGURE 3: (a) Location and layout of strain gauges; (b) overview of cement mortar specimens.

TABLE 1: Mechanical and physical parameters of cement mortar material and sandstone.

Rock type	CS (MPa)	E (GPa)	ν	ρ ($g \cdot cm^{-3}$)
Cement mortar	25.0	10.2	0.19	1.97
Sandstone	20 ~ 170	4.9 ~ 78.5	0.02 ~ 0.2	2.1

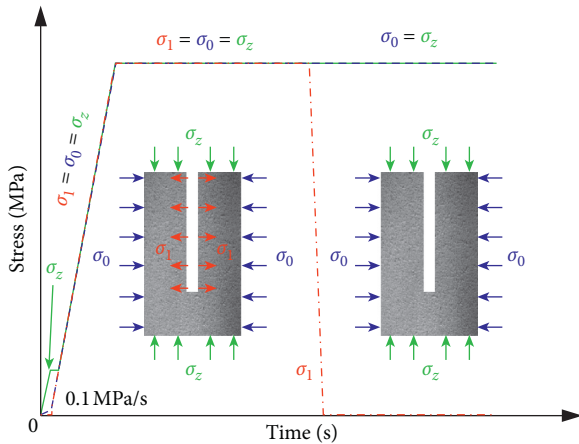


FIGURE 4: Loading, unloading paths, and stress combinations for the experimental process, where σ_1 is the internal confining stress, σ_0 is the external confining stress, and σ_z is the axial stress.

bulky piece of a slab and slices that were characterized by thinner edges and a thicker middle section peeling off from the inner sidewalls, as shown in Figures 5(c)–5(f).

It should be noted that the failure mode, caused by high deviatoric stress in unloading, was similar to the bulging failure at the tunnel face (Figure 5(d)) and the rock burst in situ field that had been observed by researchers [32], which differed from the failure mode under the loading conditions, such as axial, uniaxial, and triaxial. It was evident from Figure 6(c) that most of the deformation was observed in the

maintaining stage after unloading during the failure of the specimen. This signified that the maintaining stage after unloading was the main damage stage. Similarly, numerous studies have shown that a rockburst would occur in a period after unloading at a relatively high unloading speed [33–35]. To confirm this postulation, the AE technique was adopted to investigate the damage evolution characteristics during the test process.

3.2. Characteristics Analysis of Deformation. To clearly describe the stage test results during the entire test process, the process was divided into four sections: (I) loading stage, (II) maintaining stage after loading, (III) unloading stage, and (IV) maintaining stage after unloading. The strain response for each test after unloading is given in Figures 6 and 7. It was found from Figure 6 that the radial strain increased with the increase of the initial confining stress. When the stress was 10 MPa or 20 MPa, the radial strain response trends at the same position during the testing process were essentially the same; that is, the radial strain in the unloading stage was produced quickly, and the strain growth rate in the maintenance stage after unloading slowed down. However, the deformation after unloading was still very large, which led to the strain response in the unloading stage not being obvious in the diagram when the local stress increased to 30 MPa. It should be noted that a small deformation was detected in the unexcavated rock mass ahead of the excavation face, and it was often found in previous studies that the rock mass in a certain range ahead of the excavation face produced a small deformation under the influence of excavation unloading [36]. The strain values of the #5 to #8 strain gauges were significantly higher than those of the #1 to #4 strain gauges, respectively, indicating that the surrounding rock of the inner hollow free sidewalls might be more susceptible to excavation. Similarly, the farther away the excavation surface was, the greater the radial deformation was, and the

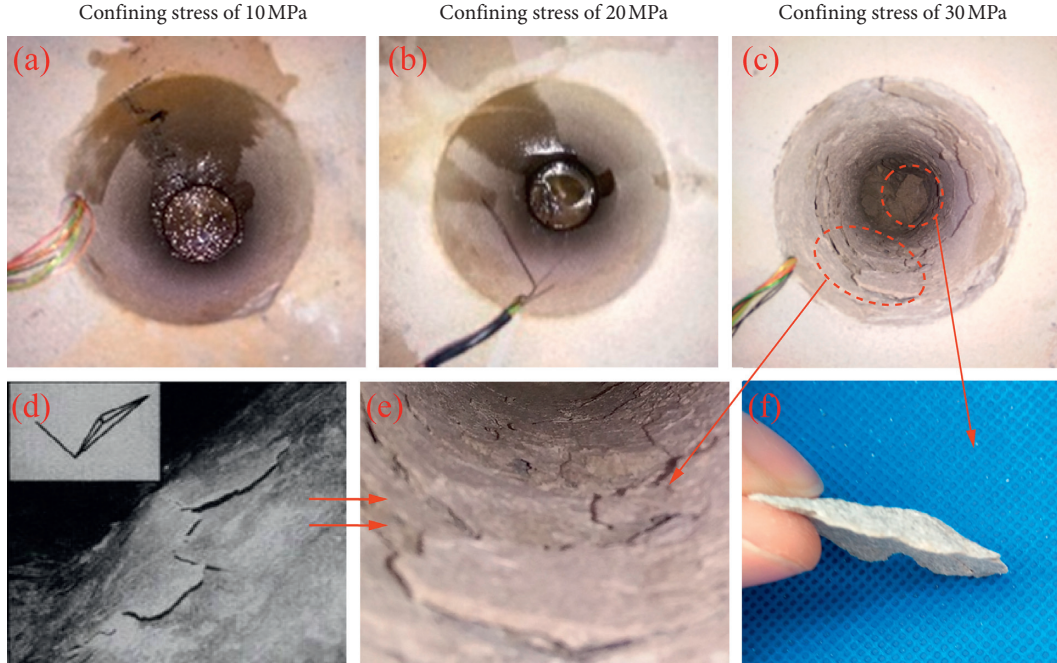


FIGURE 5: Photographs of the inner wall under initial confining stress of (a) 10, (b) 20, and (c) 30 MPa. Comparison of failure fragments in the field and test, (d) the face of the tunnel [32], (e) and (f) failure fragments of specimen.

experimental results were in accordance with the supporting theory of the excavation surface spatial effect on the rock mass around the excavation surface [37].

The slope of the strain curve was called the strain rate in this study, which indicated the speed of the deformation per unit time. It could indirectly reflect the friction and the intensity of the spatial relative position change between particles in the specimen [38], which could be written as follows:

$$\dot{\varepsilon}_r = \frac{\Delta\varepsilon_r}{\Delta t}, \quad (1)$$

where $\dot{\varepsilon}_r$ is the radial strain rate, $\Delta\varepsilon_r$ is the radial strain increment, and Δt is the time interval (in seconds).

The larger the strain rate was, the faster the deformation per unit time was. As can be seen from Figure 7, the unloading effect led to a rapid increase in deformation, and the corresponding strain curve slope was high. During the unloading stage, the strain rate increased dramatically and then decreased sharply. The strain rate generally increased with the increase of the initial confining stress. After unloading, the radial strain continued to increase and the strain rate was very small. No obvious failure of the specimen occurred when the stress was 10 MPa or 20 MPa. Nevertheless, when the stress increased to 30 MPa, the strain rate was still high and the deformation increased rapidly. During this period, the #5 strain gauge failed and the maximum strain value was $18.2 \times 10^{-3} \varepsilon$. Therefore, it was speculated that a large amount of damage accumulation occurred during the maintenance stage after the unloading, resulting in a large fracture of the sample, which is described in Section 4. It was noted that the strain rate of different strain gauges changed in an unstable manner during a period of

time after unloading. In addition, when the strain rate of some strain gauges increased suddenly at the same time, the deformation increased suddenly (Figure 7(c)), at 954 s and 1015 s. These phenomena showed that the friction and the intensity of the spatial relative position change between particles in the specimen were strengthened.

3.3. AE Characteristics. The AE events carried important information about the internal change of the material and they could reflect the fracture development and damage fracture behaviour in the rock material. Based on this, it became an important research method to predict the stress, deformation, damage, and failure evolution of rock through AE events.

3.3.1. AE Time-Domain Evolution. The AE hit was one of the AE parameters used to indicate the density and intensity of the AE activity [39]. To systematically compare the AE signals and the mechanical parameters of the test process, the AE signal and stress-strain signal were recorded at the same time at each test, so the AE and stress-strain information could correspond to each other.

Figure 8 shows the complete histograms of the AE hits for three typical specimens during the entire testing process. The total recorded times were 1181 s, 1265 s, and 1367 s. The characteristics of the AE hit signals during the entire test process included the four stages I-IV.

- (1) At the initial loading stage, the AE signals increased with the increasing load due to the loading adjustments and the closing of the original microcracks and microholes. This phenomenon has also been found in true triaxial loading experiments [34].

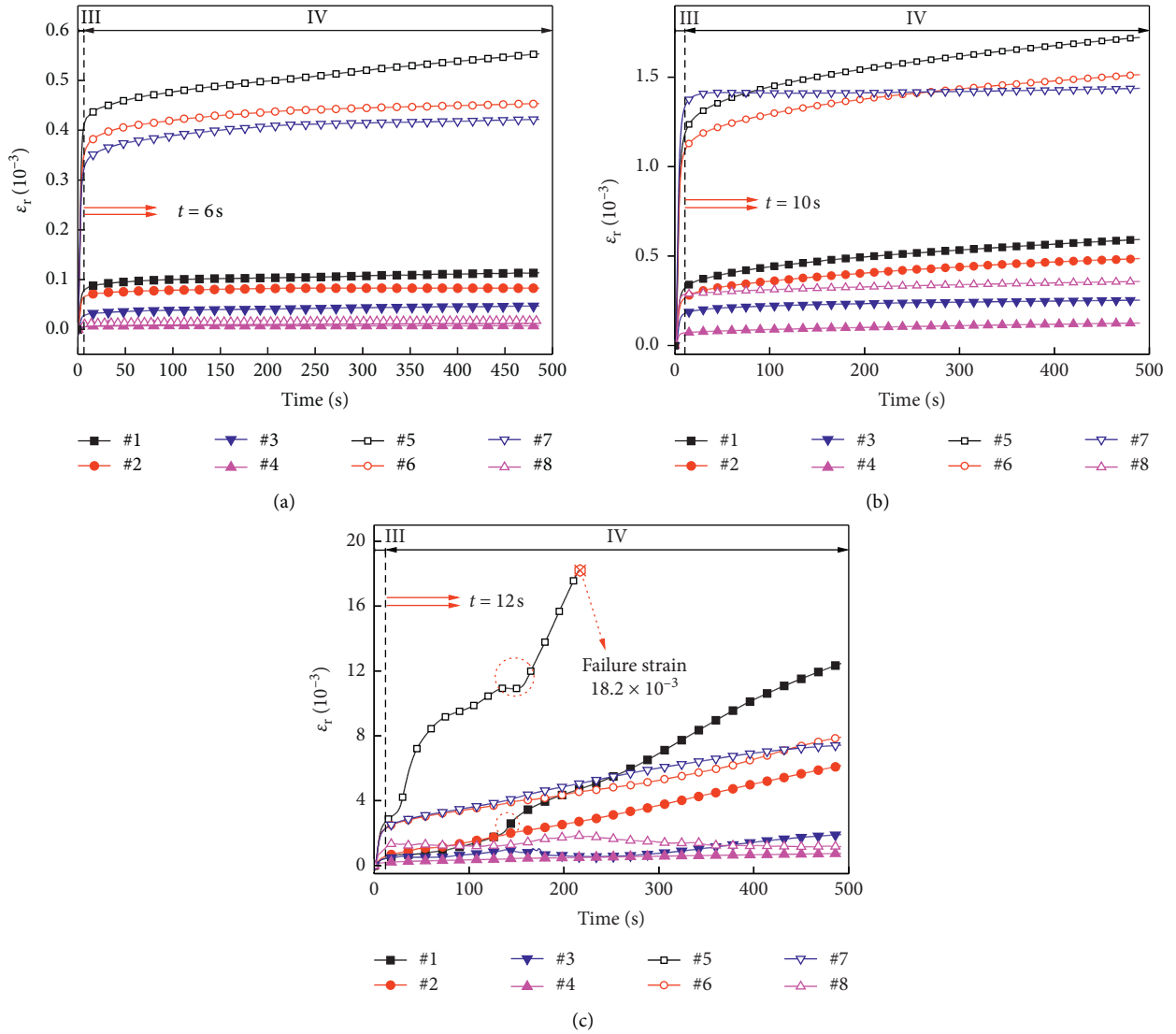


FIGURE 6: Radial deformation during unloading stage and maintaining after unloading. The unloading stage of different initial confining stress ((a) 10, (b) 20, and (c) 30 MPa) lasted for 6 s, 10 s, and 12 s, respectively. The maintaining stage of which lasted for 480 s.

- (2) At the maintenance stage after loading, the number of AE hits dropped and then stayed at a low level, and the density decreased correspondingly.
- (3) At the unloading stage, a quiescent period of AE signals occurred first. Then, the AE hits decreased after a rapid increase (Figures 8(b), 8(d), and 8(f)). During the two stages beforehand, a large amount of strain energy accumulated in the specimens. The subsequent removal of the internal confining stress in a short period of time could result in the corresponding AE hits increasing suddenly and the number of cracks increasing rapidly. The number of AE hits was still maintained at the level above the preunloading stage, and the number of cracks continued to increase. In addition, it was clear that the AE hits for the unloading stage were significantly higher than those of the loading stage. The unloading stage was the active stage of AE, and the active degree increased with the increase of the initial confining stress.
- (4) At the maintaining stage after unloading, when the stress was 10 MPa or 20 MPa, the active degree of AE decreased, but the active degree of AE was significantly higher than that in the maintaining stage after loading. When the stress was 30 MPa, a large number of AE hits occurred, the AE was still highly active in this stage, and there were three events of sharp rising and decreasing. Until the end, the hits remained at a relatively high level. The number of AE hits was closely related to the number of cracks in the specimen [40]. This meant that after unloading, the microcracks in the surrounding rock continued to produce, develop, interact, and converge into fractures. That is, the unloading effect continued to affect the surrounding rock after unloading. This also explained the phenomenon of rock burst occurring

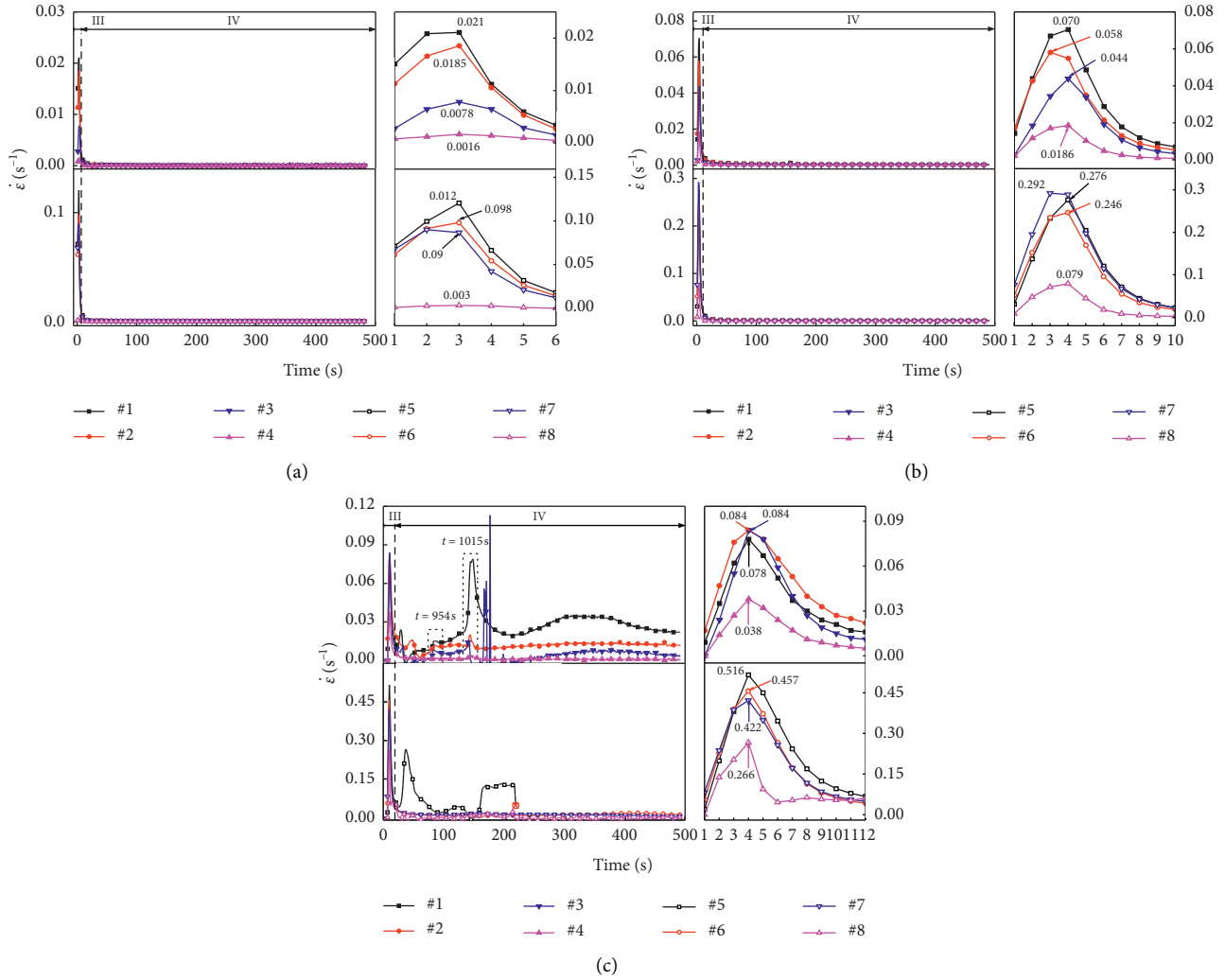


FIGURE 7: Radial strain rates during unloading stage and maintaining after unloading in different initial confining stress ((a) 10, (b) 20, and (c) 30 MPa).

after a period of time after unloading at a faster unloading speed [33–35].

As presented in Figure 8, the number of AE hits was low and high for the low initial confining stress and high initial confining stress. The larger the initial confining stress was, the greater the unloading damage was, which could cause the increase of the crack propagation speed and number of cracks. When the specimens were under relatively low initial confining stress (10 MPa and 20 MPa), the maximum AE hits occurred during the unloading stage. Nevertheless, when the stress increased to a relatively high stress (30 MPa), the maximum AE hits occurred during the maintaining stage after unloading. It should be noted that the fracture of the specimen that was caused by the stress level was not related to the time. When the stress level was constant, the unloading capacity of the main rupture of the specimen was certain. That is, the greater the in situ stress was, the higher the relative unloading capacity was when the main fracture occurred. The reason for this phenomenon may be that the greater the level of in situ stress was, the higher the degree of

compaction of the specimen was. The corresponding increase of the critical stress was caused by cracking at the crack tip, and the relative time of the occurrence of the main fracture was delayed.

3.3.2. AE Frequency-Domain Evolution. The AE waveform was transformed by fast Fourier transformation (FFT) in order to obtain the frequency spectrum information corresponding to the typical AE hits of the entire testing process. The amplitudes and the peak frequency characteristics of three typical specimens under different confining stresses are presented in Figure 9, which can be used to provide additional quantitative information about the unloading. It should be noted that the amplitude and the peak value corresponded to the AE hits at any time, which could be regarded as corresponding to the four stages:

- (1) At the initial loading stage, high-frequency and low-frequency values appeared sporadically with high amplitude.

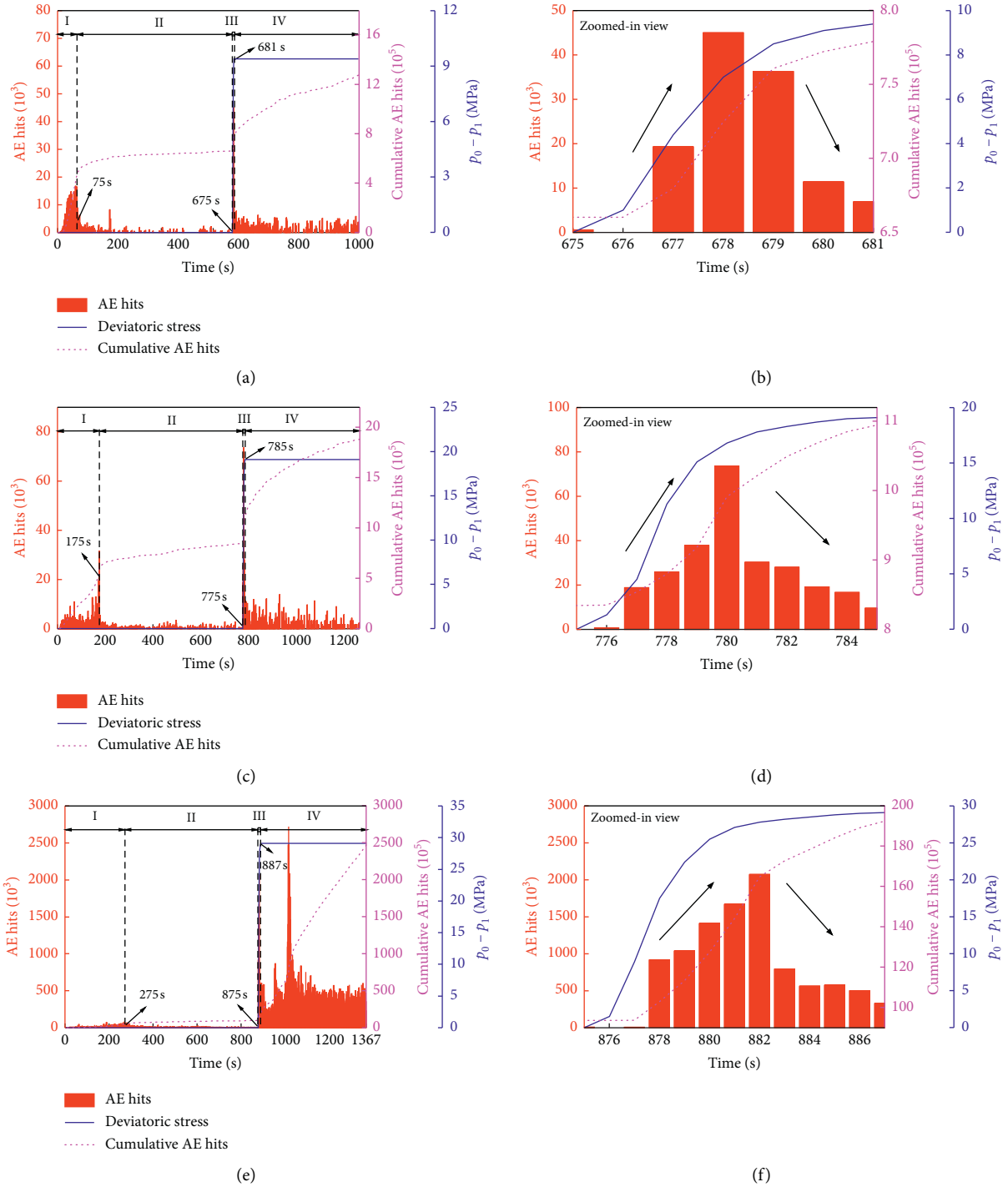


FIGURE 8: Evolution of AE hits in whole tests process for specimens under different initial confining stress ((a) and (b) 10, (c) and (d) 20, and (e) and (f) 30 MPa).

- (2) At the maintaining stage after loading, the peak frequency value and the amplitude activities of the AE signals were characterized by a sparse distribution.
- (3) At the unloading stage, the deviatoric stress increased gradually, and the peak frequency value of AE signals was characterized by a dense high amplitude distribution. The number of high-frequency

and low-frequency signals increased, and the amplitude signals clearly increased. This indicated that the cracks for different scales in the specimen increased, and the small cracks had accelerated development into large-scale fractures.

- (4) At the maintaining stage after unloading, the number of high-frequency and low-frequency

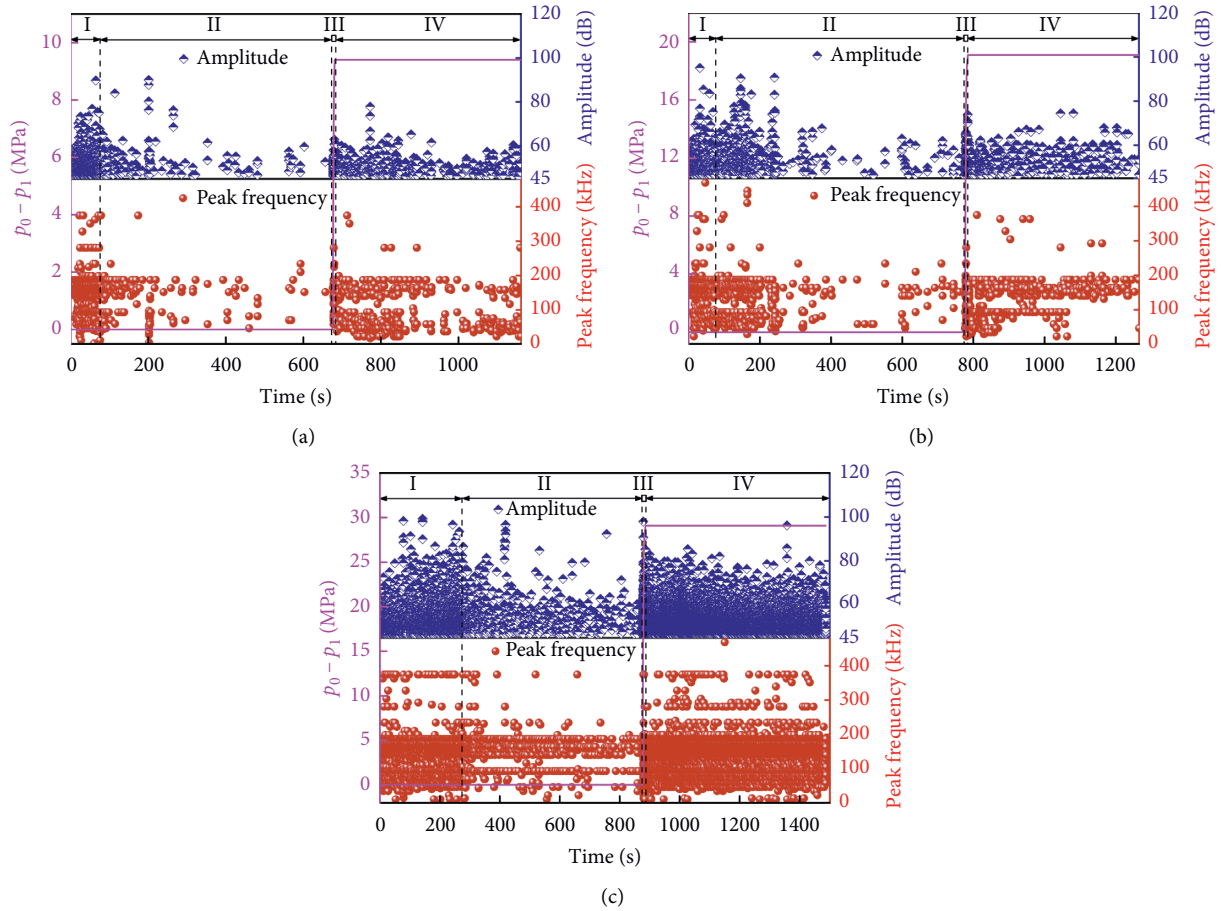


FIGURE 9: Peak frequency and amplitude of AE signals during the whole test process under different initial confining stress ((a) 10, (b) 20, (c) 30 MPa).

signals continued to increase, as did the high amplitude signals.

The peak frequency and the amplitude were distributed in a certain range (45–100 dB, 0–600 kHz) during the testing process under different initial confining stresses. It was seen that a high confining stress led to a wider frequency band and higher amplitudes. Additionally, the AE signals were characterized by a dense frequency-amplitude distribution. To facilitate the data analysis, a frequency-amplitude distribution that was recorded from the entire testing process of three typical specimens was obtained, as presented in Figure 10. Among the points of the frequency-amplitude distribution, it was evident from Figure 10 that the amplitude value of the high-frequency (>200 kHz) was much smaller than that of the low-frequency (<200 kHz). In addition, the amplitude of the high-frequency and low-frequency increased with the initial increase of the confining stress. It was obvious that there were two main frequency bands below 200 kHz, including the range of 40–100 kHz and the other range of about 140–190 kHz.

4. Damage Estimation Based on AE

4.1. AE Parameter. To facilitate the data analysis, we transformed the histograms of AE hits from the unloading

stage to maintaining stage into a continuous waveform curve in Figure 11. Bruning et al. [9] found that on the eve of the rock burst, the AE hits experienced a fast increase while it rapidly decreased after that. Su et al. [41] found that, in the process of true triaxial rock burst, the AE hits decreased rapidly after the spalling phenomenon of the free surface. Until the particle ejection, the number of AE hits increased rapidly to a high value again and then decreased. Hu et al. [21] also found that the phenomenon of particle ejection and spalling on the opening free surface corresponds to the rising point of AE hits during the rockburst process of borehole. Similarly, it was also found that AE hits enhanced sharply at the moment of the rockburst [42–44]. Therefore, combined with the failure characteristics of the specimen (Figure 5(c)), it was inferred that during the unloading and maintenance of the 30 MPa confining stress, spalling or particle ejection occurred at the corresponding three high value points of the AE hits. The damage parameter was proposed in order to investigate the damage evolution of the surrounding rock during the entire test process, as described in Section 4.2.

The changes of the AE amplitude and the strain rate during unloading under the confining stress of 30 MPa are presented in Figure 12. There was a good correspondence between the AE signal and the strain rate during this period. We found that the amplitude and the strain rate first

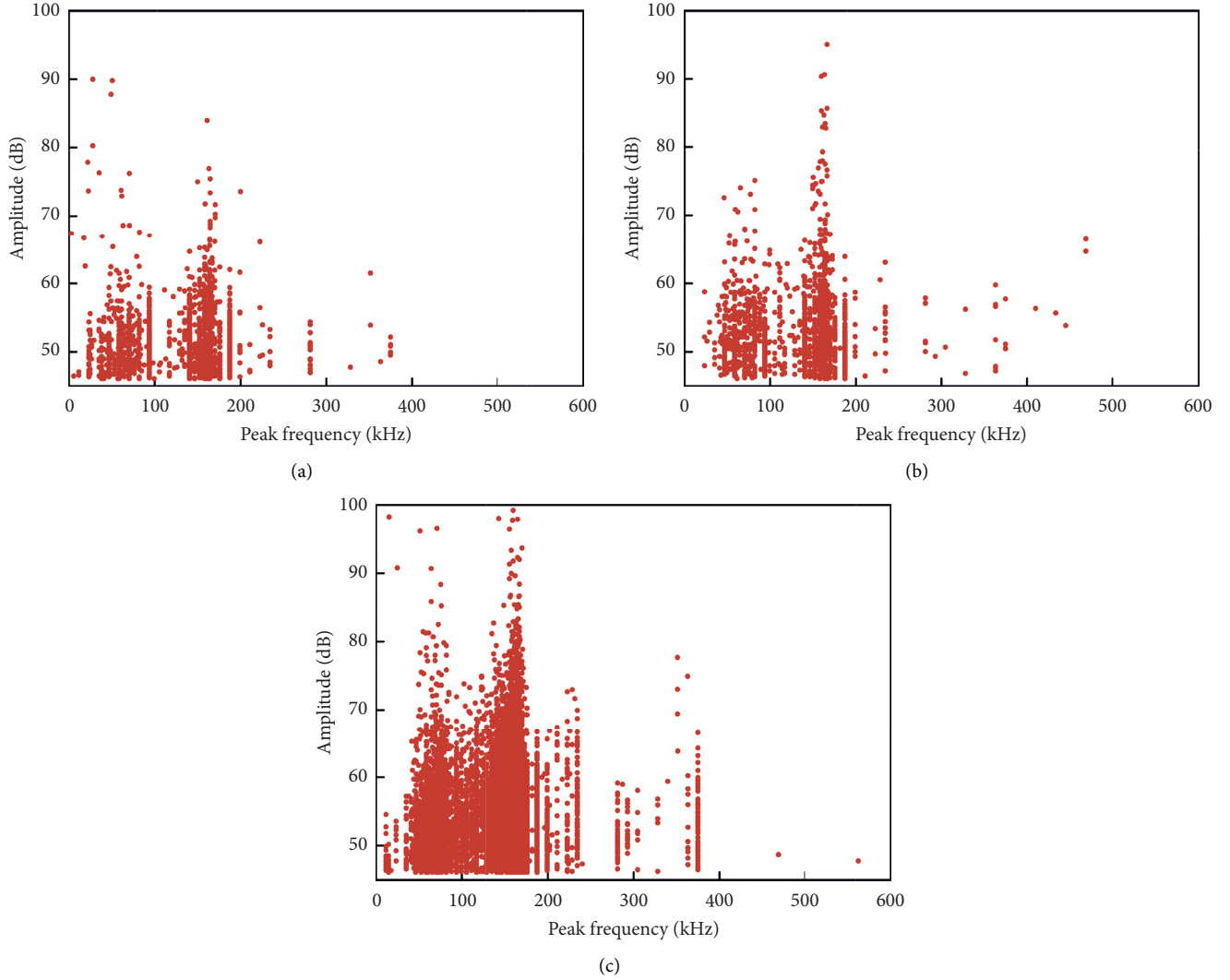


FIGURE 10: Peak frequency-amplitude distributions under different initial confining stress ((a) 10, (b) 20, (c) 30 MPa).

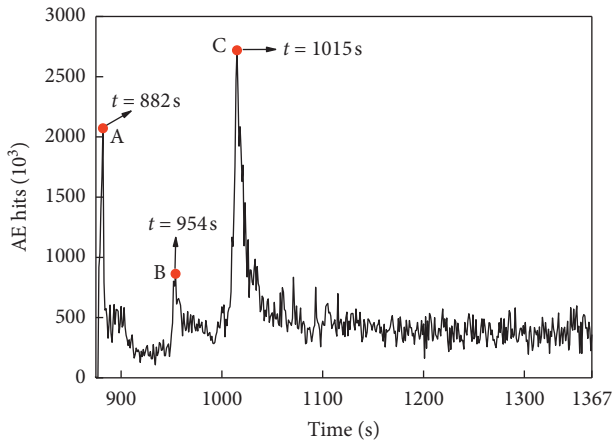


FIGURE 11: The curve of AE hits evolution after unloading under confining stress of 30 MPa.

increased and then decreased with the increase of the internal and external pressure difference during unloading. The appearance of a high strain rate was accompanied by a

high and dense amplitude signal. It was found that the amplitude of the AE signal was directly related to the size of the AE event.

4.2. Damage Parameter. The damage parameter was introduced to quantify the relative damage of the four stages involved in the test process and to investigate the progressive evolution process of the damage, and it was obtained with the following equation:

$$D_{SB} = \frac{\Omega_t}{\Omega_m}, \quad (2)$$

where D_{SB} is the damage parameter corresponding to the relative damage of specimens at any time. Ω_t is the cumulative amount of AE hits (or energy) from the start of loading to a certain time of the PHTWC specimen. Ω_m is the cumulative amount of AE hits (or energy) throughout the whole testing process. The range of values for the damage parameter D_{SB} was 0 to 1, that is, $0 \leq D_{SB} \leq 1$. It should be noted that 0 represented the cumulative amount of damage

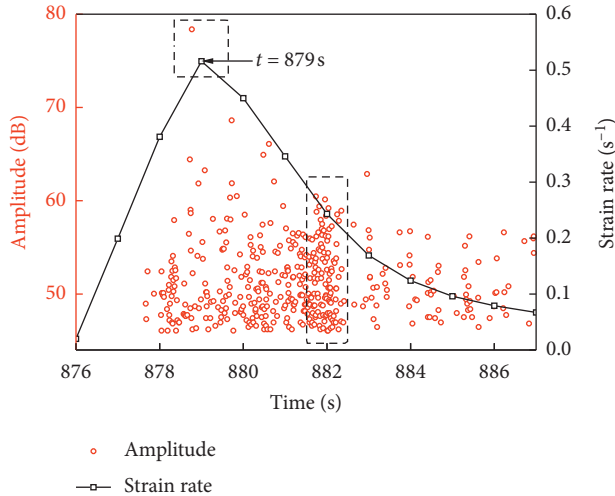


FIGURE 12: Amplitude and radial strain rate of unloading stage under confining stress of 30 MPa.

to the initial state of the test, and 1 was the amount of damage that accumulated at the end of the test, not necessarily the cumulative amount of AE in the failure state of the test piece. It is also important to note that the damage in this study referred to relative damage, which was used to investigate the damage evolution during the entire testing process for different initial confining stresses.

Equation (2) was used to establish the hypothesis that the cumulative AE hits were related to the internal damage of the specimen, so the damage evolution curves of the entire testing process for three different initial confining stresses were collected, as shown in Figure 13. It can be seen from the diagram that although the confining stress was different, the trends were essentially the same, but the damage ratio of each stage was changed. The slope of the damage curve from the OA segment increased gradually. The slope of the damage curve from the AB segment was reduced slowly. The slope of the damage curve from the BC segment was the largest, which meant that the damage per unit time was very large, although the proportion of total damage was very small. When the initial confining stress was 20 MPa, the damage ratio in the unloading stage was higher than that when the stress was 10 MPa. The longer the unloading time was, the greater the relative accumulation damage was. There was no obvious failure (Figures 5(a), 5(b)) in the specimen after unloading, which meant that the amount of relative damage in the maintenance stage after unloading was relatively lower. The slope of the CD segment decreased, but it still stayed at a high level, especially under high stress. In addition, the relative damage of this stage was much higher than the other two stresses for the stress of 30 MPa.

Overall, as the pressure level increased, points A–C on the damage curve moved down. This meant that the ratio of the damage in the maintaining stage after unloading increased, even became as high as 90% when the initial confining stress was 30 MPa. This showed that most of the damage occurred and accumulated in the maintenance stage after unloading. This verified that the unloading effect

continued to influence the surrounding rock after unloading.

4.3. *b*-Value Analysis. The change of the *b*-value was closely related to the crack scale and the stress level, which could be used to measure the development of the crack [20]. The evolution of the *b*-value with the time sequence in the unloading stage and the postunloading maintenance stage was investigated to deduce the crack development during the process of specimen failure (initial confining stress 30 MPa). The famous G-R relationship [45] from seismology was used to calculate the *b*-value with the following equation:

$$\log_{10}^N = a - bM, \quad (3)$$

where *M* is the magnitude of the earthquake, which could be replaced by the amplitude (A_{dB}) divided by 20 in the AE experiment. *N* is the cumulative number of earthquakes in the magnitude interval set in this study, which was the number of AE events. *a* and *b* are constants. During the process of changing with the time sequence, when the *b*-value tended to increase, the proportion of small events increased. In contrast, when the *b*-value tended to decrease, the proportion of large events increased.

In this study, the magnitude interval was set to 0.01 dB and the *b*-value was calculated using the least-square method. A large number of studies have shown that the different values of the calculated parameters will affect the statistical calculation results of a *b*-value. But, the variation trend is consistent as time goes on [20].

Figure 14(a) shows the rapid initiation of large new cracks corresponding to the lower initial *b*-value of unloading and the initiation of small cracks corresponding to the increase of the *b*-value with unloading. This crack initiation implied that large cracks appeared at the beginning of unloading, and then small cracks initiation and accumulation occurred. During this period, it was noted that the *b*-value experienced a decline. This indicated that small cracks accumulated and propagated, which resulted in large cracks. This corresponded to the variation of the amplitude and strain rate, as shown in Figure 12. Additionally, the amplitude was relatively high at the beginning of unloading. At 879 s, the amplitude reached the maximum value. Furthermore, at 882 s, a dense amplitude of AE signals and a large number of AE hits suddenly appeared. This indicated that more cracks existed and cracks expanded into large cracks. In general, the *b*-value increased with the increase of the internal and confining pressure difference.

The variation of the *b*-value during the maintenance stage after unloading was shown in Figure 14(b). There were two sudden decreases of the *b*-value, which meant that small cracks propagate into large cracks. During the process, the propagation of small cracks led to a continuous and unstable increase of the large fracture, and small cracks continued to increase and propagate, resulting in the emergence of large cracks. At the end of the maintaining stage, the *b*-value was kept at a high level and the small crack was steadily generated. This corresponded well to the AE hits (Figures 8(e),

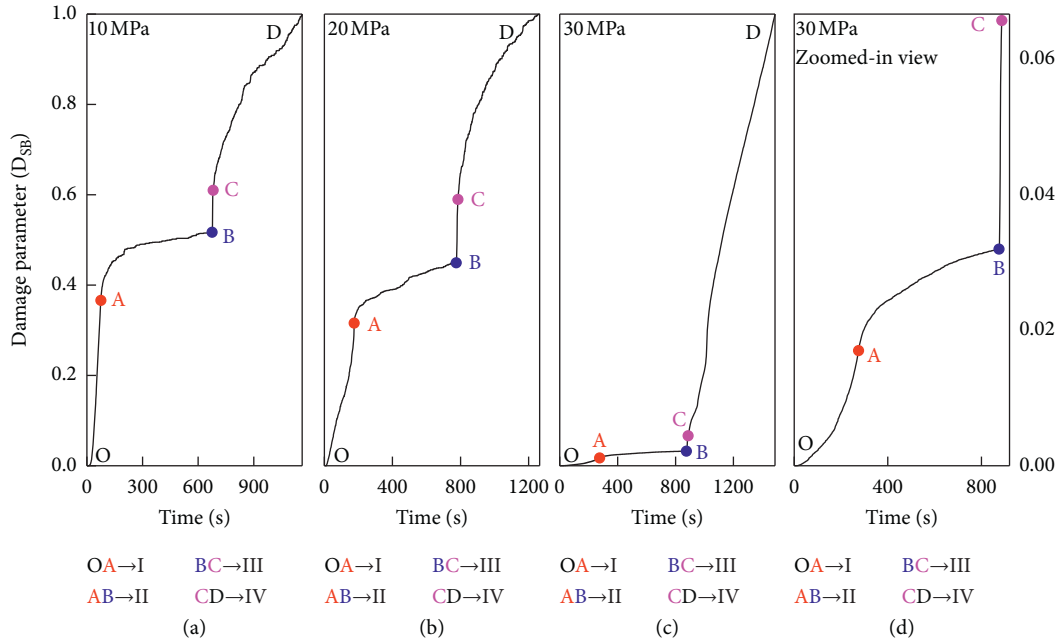


FIGURE 13: Damage evolution based on AE response under different initial confining stress ((a) 10, (b) 20, (c) 30 MPa).

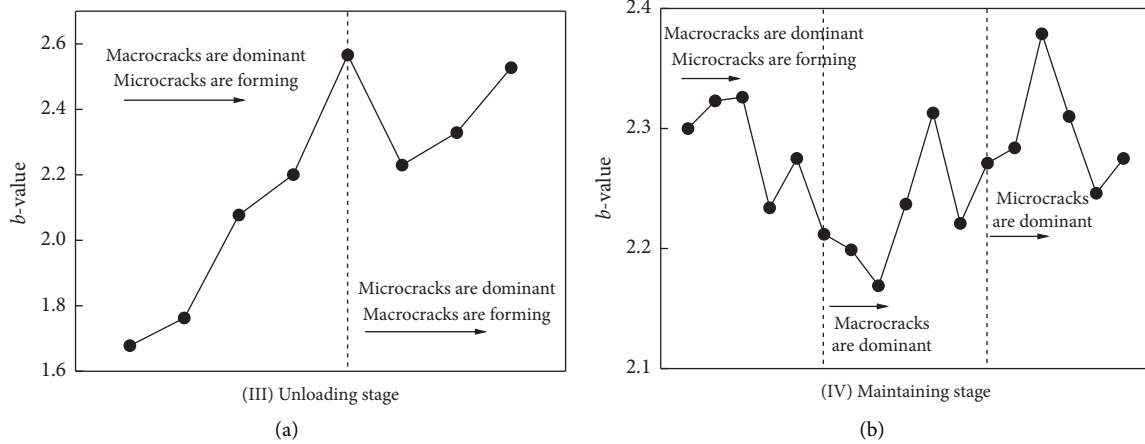


FIGURE 14: Variation of b -value in the process of failure under confining stress of 30 MPa: (a) unloading stage and (b) maintaining stage after unloading.

8(f)), and large numbers of AE hits appeared at about 954 s and 1015 s.

5. Conclusions

- (1) At the unloading stage, the strain rates and the AE hits for different stress levels were characterized by decreasing after an initial increase. At the maintaining stage after unloading, when the specimens were under a relatively low initial confining stress (10 MPa, 20 MPa), the radial strain rates were very small. In contrast, when the stress increased to a relatively high stress (30 MPa), the rates were unstable, which implied that the local and regional damage failures of the surrounding rocks near or at the opening free surface were occurring.

- (2) It was seen that the rock failure behaviour was triggered by a relatively high deviatoric stress level in this study. The higher stress level accelerated the damage development caused by the unloading effect and increased the expansion rate of the internal cracks, so the AE hits increased.
- (3) The amplitudes of the high-frequency or low-frequency increased with the initial increase of the confining stress. In addition, the amplitude value of the high-frequency (>200 kHz) was much smaller than that of the low-frequency (<200 kHz). Two main frequency bands below 200 kHz were presented, including the range of 40–100 kHz and the range of about 140–190 kHz.
- (4) For a faster unloading rate condition, large cracks occurred at the beginning of unloading, followed by

small cracks initiation and accumulation. The evolution of the squeezing deformation and the failure occurred along with the increase of the unloading damage. Based on the proposed damage parameter, the damage mainly occurred in the maintenance stage after unloading. That is, the unloading effect continued to affect the surrounding rock after unloading.

Data Availability

The data used to support the findings of this study are available from the corresponding author upon request.

Conflicts of Interest

The authors declare that there are no conflicts of interest.

Acknowledgments

This work was supported by the National Key Project of National Natural Science Foundation and Shenhua Group Corporation Limited of China (U1361210) and the National Nature Science Foundation of China (51574247).

References

- [1] M. Cai and P. K. Kaiser, "In-situ rock spalling strength near excavation boundaries," *Rock Mechanics and Rock Engineering*, vol. 47, no. 2, pp. 659–675, 2014.
- [2] L. Cantieni and G. Anagnostou, "The effect of the stress path on squeezing behavior in tunneling," *Rock Mechanics and Rock Engineering*, vol. 42, no. 2, pp. 289–318, 2009.
- [3] W. D. Ortlepp, *Rock Fracture and Rockbursts: An Illustrative Study*, pp. 37–54, Journal of the Southern African Institute of Mining and Metallurgy, Johannesburg, South Africa, 1997.
- [4] P. K. Kaiser, D. D. Tannant, and D. R. McCreath, *Canadian Rockburst Support Handbook*, pp. 66–81, Geomech Res Centre, Laurentian University, Sudbury, Canada, 1996.
- [5] E. Hoek and C. D. Martin, "Fracture initiation and propagation in intact rock—a review," *Journal of Rock Mechanics and Geotechnical Engineering*, vol. 6, no. 4, pp. 287–300, 2014.
- [6] Q. Jiang, X. T. Feng, T. B. Xiang, and G. S. Su, "Rockburst characteristics and numerical simulation based on a new energy index: a case study of a tunnel at 2,500 m depth," *Bulletin of Engineering Geology and the Environment*, vol. 69, no. 3, pp. 381–388, 2010.
- [7] A. Taheri, Y. Zhang, and H. Munoz, "Performance of rock crack stress thresholds determination criteria and investigating strength and confining pressure effects," *Construction and Building Materials*, vol. 243, Article ID 118263, 2020.
- [8] S. Ghasemi, M. Khamsehchiyan, A. Taheri, M. R. Nikudel, and A. Zalooli, "Crack evolution in damage stress thresholds in different minerals of granite rock," *Rock Mechanics and Rock Engineering*, vol. 53, no. 3, pp. 1163–1178, 2020.
- [9] T. Bruning, M. Karakus, G. D. Nguyen, and D. Goodchild, "Experimental study on the damage evolution of brittle rock under triaxial confinement with full circumferential strain control," *Rock Mechanics and Rock Engineering*, vol. 51, no. 11, pp. 3321–3341, 2018.
- [10] Q. L. Wu, A. Z. Lü, Y. T. Gao, S. C. Wu, and N. Zhang, "Stress analytical solution for plane problem of a double-layered thick-walled cylinder subjected to a type of non-uniform distributed pressure," *Journal of Central South University*, vol. 21, no. 5, pp. 2074–2082, 2014.
- [11] M. Saadat and A. Taheri, "Modelling micro-cracking behaviour of pre-cracked granite using grain-based distinct element model," *Rock Mechanics and Rock Engineering*, vol. 52, no. 11, pp. 4669–4692, 2019.
- [12] M. Saadat and A. Taheri, "A numerical approach to investigate the effects of rock texture on the damage and crack propagation of a pre-cracked granite," *Computers and Geotechnics*, vol. 111, pp. 89–111, 2019.
- [13] L. Weng, X. Li, A. Taheri, Q. Wu, and X. Xie, "Fracture evolution around a cavity in brittle rock under uniaxial compression and coupled static-dynamic loads," *Rock Mechanics and Rock Engineering*, vol. 51, no. 2, pp. 531–545, 2018.
- [14] H. Munoz and A. Taheri, "Post-peak deformability parameters of localised and non-localised damage zones of rocks under cyclic loading," *Geotechnical Testing Journal*, vol. 42, no. 6, pp. 1663–1684, 2019.
- [15] H. Munoz and A. Taheri, "Specimen aspect ratio and progressive field strain development of sandstone under uniaxial compression by three-dimensional digital image correlation," *Journal of Rock Mechanics and Geotechnical Engineering*, vol. 9, no. 4, pp. 599–610, 2017.
- [16] K. Mogi, "Study of elastic shocks caused by the fracture of heterogeneous materials and its relations to earthquake phenomena," *Bulletin of the Earthquake Research Institute*, vol. 40, pp. 125–173, 1962.
- [17] J. Kaiser, "Erkenntnisse und Folgerungen aus der Messung von Geräuschen bei Zugbeanspruchung von metallischen Werkstoffen," *Archiv für das Eisenhüttenwesen*, vol. 24, no. 1–2, pp. 43–45, 1953.
- [18] S. Q. Qin and Z. D. Li, *Introduction to Rock Acoustic Emission Technology*, Southwest Jiaotong University Press, Chengdu, China, 1993.
- [19] D. J. Holcomb, "General theory of the Kaiser effect," *International Journal of Rock Mechanics and Mining Sciences & Geomechanics Abstracts*, vol. 30, no. 7, pp. 929–935, 1993.
- [20] J. S. Kim, K. S. Lee, W. J. Cho, H. J. Choi, and G. C. Cho, "A comparative evaluation of stress-strain and acoustic emission methods for quantitative damage assessments of brittle rock," *Rock Mechanics and Rock Engineering*, vol. 48, no. 2, pp. 495–508, 2015.
- [21] X. Hu, G. Su, G. Chen et al., "Experiment on rockburst process of borehole and its acoustic emission characteristics," *Rock Mechanics and Rock Engineering*, vol. 52, no. 3, pp. 783–802, 2019.
- [22] Y. J. Yang, D. C. Wang, M. F. Guo, and B. Li, "Study of rock damage characteristics based on acoustic emission tests under triaxial compression," *Chinese Journal of Rock Mechanics and Engineering*, vol. 33, no. 1, pp. 98–104, 2014.
- [23] Z. Zhang, R. Zhang, H. Xie, J. Liu, and P. Were, "Differences in the acoustic emission characteristics of rock salt compared with granite and marble during the damage evolution process," *Environmental Earth Sciences*, vol. 73, no. 11, pp. 6987–6999, 2015.
- [24] N. C. Gay, "Fracture growth around openings in thick-walled cylinders of rock subjected to hydrostatic compression," *International Journal of Rock Mechanics and Mining Sciences & Geomechanics Abstracts*, vol. 10, no. 3, pp. 209–233, 1973.
- [25] M. I. Alsayed, "Utilising the Hoek triaxial cell for multiaxial testing of hollow rock cylinders," *International Journal of Rock Mechanics and Mining Sciences*, vol. 39, no. 3, pp. 355–366, 2002.
- [26] D. H. Lee, C. H. Juang, H. M. Lin, and S. H. Yeh, "Mechanical behavior of Tien-Liao mudstone in hollow cylinder tests,"

- Canadian Geotechnical Journal*, vol. 39, no. 3, pp. 744–756, 2002.
- [27] H. Q. Zhang, H. G. Liu, Y. N. He, and L. J. Han, “Unloading experiment and rock strength failure of rock thick-walled cylinders under triaxial compression,” *Journal of University of Science and Technology Beijing*, vol. 33, no. 7, pp. 800–805, 2011.
- [28] V. Labiouse, C. Sauthier, and S. You, “Hollow cylinder simulation experiments of galleries in boom clay formation,” *Rock Mechanics and Rock Engineering*, vol. 47, no. 1, pp. 53–55, 2014.
- [29] G. Y. Hou, X. R. Li, Z. D. Zhang, H. Y. Liang, and J. C. Zhang, “Experimental system for simulating excavation unloading process of rock around roadway by using small cylindrical hollow specimen,” *Chinese Journal of Rock Mechanics and Engineering*, vol. 36, no. 9, pp. 2136–2145, 2017.
- [30] S. Wang, X. Li, K. Du, S. Wang, and M. Tao, “Experimental study of the triaxial strength properties of hollow cylindrical granite specimens under coupled external and internal confining stresses,” *Rock Mechanics and Rock Engineering*, vol. 51, no. 7, pp. 2015–2031, 2018.
- [31] G. Y. Hou, J. P. Liang, M. H. Zhou, and Y. K. Cui, “Experimental study on effect of unloading velocity on surrounding rock deformation,” *Journal of China Coal Society*, vol. 44, no. 4, pp. 1011–1019, 2019.
- [32] C. D. Martin, R. S. Read, and J. B. Martino, “Observations of brittle failure around a circular test tunnel,” *International Journal of Rock Mechanics and Mining Sciences*, vol. 34, no. 7, pp. 1065–1073, 1997.
- [33] A. M. Linkov, “Rockbursts and the instability of rock masses,” *International Journal of Rock Mechanics and Mining Sciences & Geomechanics Abstracts*, vol. 33, no. 7, pp. 727–732, 1996.
- [34] X. G. Zhao, J. Wang, M. Cai et al., “Influence of unloading rate on the strainburst characteristics of beishan granite under true-triaxial unloading conditions,” *Rock Mechanics and Rock Engineering*, vol. 47, no. 2, pp. 467–483, 2014.
- [35] X. B. Li, Z. H. Chen, W. Z. Cao, M. Tao, and J. Zhou, “Time-effect properties and mechanisms of marble failure under different unloading rates,” *Chinese Journal of Geotechnical Engineering*, vol. 39, no. 9, pp. 1565–1574, 2017.
- [36] T. Unlu and H. Gercek, “Effect of Poisson’s ratio on the normalized radial displacements occurring around the face of a circular tunnel,” *Tunnelling and Underground Space Technology*, vol. 18, no. 5, pp. 547–553, 2003.
- [37] H. Basarir, M. Genis, and A. Ozarslan, “The analysis of radial displacements occurring near the face of a circular opening in weak rock mass,” *International Journal of Rock Mechanics and Mining Sciences*, vol. 47, no. 5, pp. 771–783, 2010.
- [38] X. Gao, S. J. Liu, J. W. Huang, Z. C. Yang, W. F. Mao, and L. X. Wu, “The influence of strain rate on AE characteristics during rock deformation,” *Chinese Journal of Rock Mechanics and Engineering*, vol. 37, no. 4, pp. 887–897, 2018.
- [39] C. U. Grosse and M. Ohtsu, *Acoustic Emission Testing*, Springer, Berlin, Heidelberg, Germany, 2008.
- [40] Z. Moradian, H. H. Einstein, and G. Ballivy, “Detection of cracking levels in brittle rocks by parametric analysis of the acoustic emission signals,” *Rock Mechanics and Rock Engineering*, vol. 49, no. 3, pp. 785–800, 2016.
- [41] G. Su, Y. Shi, X. Feng, J. Jiang, J. Zhang, and Q. Jiang, “True-triaxial experimental study of the evolutionary features of the acoustic emissions and sounds of rockburst processes,” *Rock Mechanics and Rock Engineering*, vol. 51, no. 2, pp. 375–389, 2018.
- [42] M. C. He, J. L. Miao, and J. L. Feng, “Rock burst process of limestone and its acoustic emission characteristics under true-triaxial unloading conditions,” *International Journal of Rock Mechanics and Mining Sciences*, vol. 47, no. 2, pp. 286–298, 2010.
- [43] M. He, H. Xia, X. Jia, W. Gong, F. Zhao, and K. Liang, “Studies on classification, criteria and control of rockbursts,” *Journal of Rock Mechanics and Geotechnical Engineering*, vol. 4, no. 2, pp. 97–114, 2012.
- [44] M. C. He, F. Zhao, M. Cai, and S. Du, “A novel experimental technique to simulate pillar burst in laboratory,” *Rock Mechanics and Rock Engineering*, vol. 48, no. 5, pp. 1833–1848, 2015.
- [45] B. Gutenberg and C. F. Richter, “Frequency of earthquakes in California,” *Bulletin of the Seismological Society of America*, vol. 34, no. 4, pp. 185–188, 1944.